Nano Research
2019, 12(7): 1675–1681

ISSN 1998-0124 CN 11-5974/O4
https://doi.org/10.1007/s12274-019-2421-9

Research Article

Atomic-scale structural and chemical evolution of $Li_3V_2(PO_4)_3$ cathode cycled at high voltage window

Shulin Chen[1,2,3], Jian Zou[1], Yuehui Li[3], Ning Li[3], Mei Wu[3], Jinghuang Lin[2], Jingmin Zhang[3], Jian Cao[2], Jicai Feng[2], Xiaobin Niu[1], Jianming Bai[4], Junlei Qi[2] (✉), Peng Gao[2,3,5,6] (✉), Liping Wang[1] (✉), and Hong Li[7]

[1] *School of Materials and Energy, State Key Laboratory of Electronic Thin Film and Integrated Devices, University of Electronic Science and Technology of China, Chengdu 610054, China*
[2] *State Key Laboratory of Advanced Welding and Joining, Harbin Institute of Technology, Harbin 150001, China*
[3] *Electron Microscopy Laboratory, School of Physics, Peking University, Beijing 100871, China*
[4] *National Synchrotron Light Source II, Brookhaven National Laboratory, Upton, New York 11973, USA*
[5] *Collaborative Innovation Center of Quantum Matter, Beijing 100871, China*
[6] *International Center for Quantum Materials, School of Physics, Peking University, Beijing 100871, China*
[7] *Institute of Physics, Chinese Academy of Sciences, Beijing 100190, China*

Received: 6 February 2019 / **Revised:** 14 March 2019 / **Accepted:** 21 April 2019

ABSTRACT

Here, by using atomically resolved scanning transmission electron microscopy and electron energy loss spectroscopy, we investigate the structural and chemical evolution of $Li_3V_2(PO_4)_3$ (LVP) upon the high-voltage window (3.0–4.8 V). We find that the valence of vanadium gradually increases towards the core corresponding to the formation of electrochemically inactive $Li_{3-x}V_2(PO_4)_3$ ($L_{3-x}VP$) phases. These Li-deficient phases exhibit structure distortion with superstructure stripes, likely caused by the migration of the vanadium, which can slow down the lithium ion diffusion or even block the diffusion channels. Such kinetic limitations lead to the formation of Li-deficient phase along with capacity loss. Thus, the LVP continuously losses of electrochemical activity and Li-deficient phases gradually grow from the particle core towards the surface during cycling. After 500 cycles, the thickness of active LVP layer decreases to be ~ 5–20 nm. Moreover, the micromorphology and chemical composition of solid electrolyte interphase (SEI) have been investigated, indicating the thick SEI film also contributes to the capacity loss. The present work reveals the structural and chemical evolution in the cycled electrode materials at an atomic scale, which is essential to understand the voltage fading and capacity decaying of LVP cathode.

KEYWORDS

lithium-ion batteries, Li-deficient lithium vanadium phosphate, capacity fading, solid electrolyte interphase, scanning transmission electron microscopy, electron energy loss spectroscopy

1 Introduction

The ever-growing demand for rechargeable lithium ion batteries in portable electronics and electric vehicles requires the next generation electrode materials featured with high energy and power delivery along with long cycling life [1]. One way to improve the energy and power densities is to increase the output voltage while maintaining a high capacity with long-term operations [2]. Among the cathode materials, lithium vanadium phosphate $Li_3V_2(PO_4)_3$ (LVP) with a monoclinic structure has attracted extensive research attention due to the high theoretical specific capacity (197 $mAh \cdot g^{-1}$), high average working potential around 4.0 V vs. Li^+/Li [3–5]. When charged to 4.3 V, three plateaus can be observed corresponding to three successive two-phase transition processes: $Li_3V_2(PO_4)_3$ to $Li_{2.5}V_2(PO_4)_3$ at 3.6 V, $Li_{2.5}V_2(PO_4)_3$ to $Li_2V_2(PO_4)_3$ at 3.7 V, $Li_2V_2(PO_4)_3$ to $Li_1V_2(PO_4)_3$ at 4.1 V. When the last Li^+ is extracted ($Li_1V_2(PO_4)_3$ to $V_2(PO_4)_3$) at around 4.5 V, a slopy discharge–charge curve is observed, indicating a solid-solution behavior [6]. The practical application of LVP remains hindered by its low initial coulombic efficiency, capacity fading issues and poor high rate performance, especially cycling at a high voltage window 3.0–4.8 V [7]. Cycling in a high voltage window can lead to side reactions and thermodynamic instability, which can break the desirable crystal and electronic structures that allow for electrons and ions transport to achieve redox reactions. Despite that various strategies have been adopted to improve the cycling performance including carbon coating [8, 9], nano-crystallization [10, 11], and element doping [12], the capacity fading issue still exists after extended cycles. Thus, it is of great importance to probe the battery degradation mechanism with the aim of better designing the electrode materials.

To achieve a stable cycling performance for cathode, it is vital to maintain the crystal and electronic structures, which ensures the efficient transport of the electrons and ions for the redox reactions. From *in situ* X-ray diffraction (XRD), Yoon et al. found the LVP cathode returns to be $Li_{2.5}V_2(PO_4)_3$ rather than LVP after one cycle in 3.0–4.8 V, which can also be confirmed by their X-ray absorption near edge structure results [13]. Moreover, by *in situ* X-ray absorption spectroscopy (XAS), Kim et al. also observed the average valence of vanadium (+3.73–3.84) for LVP after one cycle is higher than the expected +3 [14]. After cycling, Min et al. found the volume of LVP expanded irreversibly, responsible for the capacity fading [15]. Contrary to these findings about the structural irreversibility, Kang

Address correspondence to Junlei Qi, jlqi@hit.edu.cn; Peng Gao, p-gao@pku.edu.cn; Liping Wang, lipingwang@uestc.edu.cn

et al. observed the structure of LVP can be fully recovered after one cycle in 3.0–4.8 V based on *in situ* XRD [16]. Also, Wang et al. demonstrated both V–O and V–P distances can recover to the pristine values, suggesting reversible local structure change [17]. These studies show contradictory results about the structure reversibility for LVP cycled in 3.0–4.8 V, which is likely because these bulk-sensitive techniques only provide an average structure or chemical information, easily losing some local inhomogeneity information. Transmission electron microscopy (TEM) with a high resolution has the rich imaging and powerful spectroscopic functions [18], which allows us to identify the localized structure reconstruction or distortion and measure the localized chemical compositions and valence. For example, we can investigate the mechanical fracture [19], the migration of transition metal ions [20], and surface structural reconstruction [21], which are all related with the failure in batteries cycled to a high voltage [22–24] but are largely remaining unexplored for LVP. Thus, it is urgent to reveal these microscopic changes to better understand the relationships between the structure and properties for LVP cathode and thus guide material designs.

In this work, we mainly investigate the structural and the chemical evolution of LVP cycled in a high voltage window 3.0–4.8 V by using aberration corrected scanning transmission electron microscopy (STEM) and the electron energy loss spectroscopy (EELS). We find that the LVP suffers from a serious capacity fading after 500 cycles in 3.0–4.8 V while a good capacity retention and rate performance are observed when cycled in 3.0–4.3 V. The capacity fading at a high voltage window is mainly attributed to the formation of massive electrochemically inactive Li-deficient phases as well as a thick SEI layer. We find the valence of vanadium gradually increases towards the inner part, indicating that the inactive Li-deficient phase initially forms in the core while surface phase LVP remains active. The width of LVP surface layer decreases to be only ~ 5–20 nm after 500 cycles. Such Li-deficient phase is likely caused by the migration of vanadium, which may slow down the lithium ion diffusion or even block the diffusion channels. The kinetic limitations lead to the loss of electrochemical activity along with the capacity loss. Moreover, the thickness of the solid electrolyte interphase (SEI) layer ranges from 48 to 113 nm of LVP after 500 cycles in 3.0–4.8 V while the thickness is about 20 nm when cycled in 3.0–4.3 V. The thick SEI layer also contributes to the capacity loss. Our observations help to better understand the main origins of the capacity fading of LVP and emphasize that maintaining structure stability is the key step towards high-voltage cathode materials.

2 Experimental

2.1 Material synthesis and characterization

The LVP was synthesized by a conventional solid-state reaction route. The starting materials include analytical grade Li_2CO_3 (0.0157 mol, 1.165 g), NH_4VO_3 (0.02 mol, 2.339 g), $NH_4H_2PO_4$ (0.03 mol, 3.451 g) and citric acid (1.710 g). Citric acid here was used as the carbon precursor to obtain carbon coated LVP (LVP/C) to improve the intrinsically low electronic conductivity. After a high energy ball-milling process at 300 rounds per minute for 12 h, the mixture was annealed at 700 °C for 10 h under Ar/H_2 (9:1) atmosphere at a heating ramp of 5 °C·min^{-1}.

Powder X-ray diffraction (PXRD) patterns were obtained on a D8 Advance diffractometer using Cu Kα radiation ($\lambda_{Cu\text{-}K\alpha1}$ = 1.54056 Å, $\lambda_{Cu\text{-}K\alpha2}$ = 1.54439 Å). Scanning electron microscopy (SEM) images of the sample morphologies were examined by FEI NanoSEM 430. TEM images were acquired using Tecnai F20 at 200 kV. High-angle annular dark field (HAADF) STEM images, energy dispersive X-ray spectroscopy (EDS), and EELS were acquired at an aberration corrected FEI (Titan Cubed Themis G2) equipped with an X-FEG gun, a Bruker Super-X EDS detector and Gatan Enfinium ER spectrometer, operated at 300 kV. Under STEM mode, the convergence semi-angle is 21 mrad, the collection semi-angle snap is in the range of 80–380 mrad and the beam current is 80 pA. EELS semi-collection angle is 21 mrad. EELS spectra dispersion is 0.25 eV per channel. The EELS line scan was acquired with the 1 nm for each step. The background of core loss has been processed using power law and cubic curves with Lorentz peak.

2.2 Electrochemical measurements

For the preparation of the battery electrode, the slurry was prepared by mixing active LVP/C composite (80 wt.%), carbon black (10 wt.%), and polyvinylidene fluoride (PVDF, 10 wt.%) in N-methylpyrrolidone (NMP) solvent. The slurry was then cast onto a clear Al foil before drying in vacuum at 80 °C for 12 h. The loading of the electrode materials was approximately 2.0 mg·cm^{-2}. An electrolyte (1 M $LiPF_6$; ethylene carbonate (EC):dimethyl carbonate (DMC) = 50:50 (v:v) was used for the lithium ion batteries. 2032-type stainless steel coin cells were assembled in an argon-filled glovebox (O_2 < 0.1 ppm; H_2O < 0.1 ppm). The batteries were galvanostatically charged and discharged on a LAND CT2001A cell test apparatus at room temperature. The electrochemical impedance spectroscopy (EIS) was carried out on electrochemical workstation (Bio-Logic) with an amplitude of 5 mV in the frequency range 10^{-2}–10^5 Hz. All the measurements were carried out with a two-electrode system at room temperature. For preparing *ex situ* samples after cycled 500 times, the obtained electrodes were immersed in DMC for 12 h and then washed with DMC for 3 times to clean the residue electrolyte. Then the electrodes were separated with the Al foil and grounded to be fine powders. The powders were dispersed in alcohol and then dropped onto the holey carbon copper girds for TEM characterizations.

3 Results and discussion

To improve the intrinsically low electronic conductivity of the LVP, we intentionally coated a carbon layer around LVP. The thickness of the carbon layer is about 5–10 nm as shown in Fig. S1(a) in the Electronic Supplementary Material (ESM). The carbon content is measured to be ~ 8.6 wt.% as the thermo gravimetric analyzer (TGA) test shows in Fig. S1(b) in the ESM. The SEM image in Fig. 1(a) shows the as-synthesized LVP/C ranges in size ~ 0.5–1 μm across. The STEM image in Fig. 1(b) shows a regular outlook of LVP/C, indicating a good crystalline. The crystalline is further inspected by the selected area electron diffraction (SAED) in Fig. 1(c) along the [1$\bar{1}$1] direction. The Rietveld refinement of the XRD pattern in Fig. 1(d) confirms that we have obtained the phase-pure LVP powders with a monoclinic structure (space group $P21/n$; a = 8.61092 Å, b = 8.61004 Å, c = 12.05157 Å; $\alpha = \gamma$ = 90.0000°, β = 90.5380°). Note that there is no evidence of carbon diffraction peaks, indicating the coated carbon is likely amorphous, which can also be confirmed by the TEM image in Fig. S1(a) in the ESM. The arrangement of the transition metal vanadium is atomically resolved along the [20$\bar{1}$] zone axis in Fig. 1(e). Note that the Li, O and P atoms are not identified due to their light atomic masses. The electronic structure is probed using the STEM-EELS in Fig. 1(f) wherein the V-K edge and the O-L edge are identified. The elements of V, P, O, and C distribute uniformly as the EDS mappings show (Fig. S2 in the ESM). The above results show that a single pure phase LVP/C has been successfully synthesized.

The electrochemical performances of the LVP/C cathode were investigated. Distinct electrochemical behaviors are observed between a lower voltage window 3.0–4.3 V and a higher voltage window 3.0–4.8 V. When cycled at 0.2 C in the voltage range 3.0–4.8 V, the capacity gradually decreases (Figs. 2(a) and 2(b)), while the capacity fading is slight during the cycles in 3.0–4.3 V at 0.2 C (Fig. 2(c)). After 500 cycles, the discharge specific capacity decreases largely

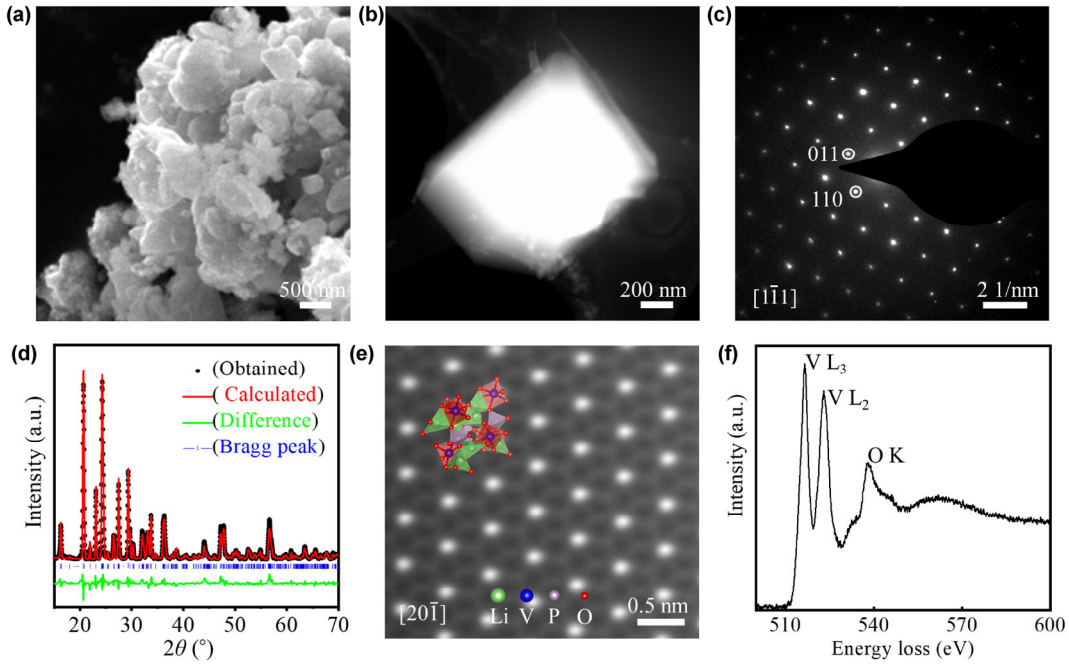

Figure 1 The crystal structure and electronic structure of the pristine LVP/C. (a) A SEM image, (b) a STEM image, (c) a SAED pattern viewing from the [1$\bar{1}$1] direction. (d) The Rietveld refinement of the XRD pattern of the as-obtained LVP with observed data (black points), calculated data (red line), difference (green line) and Bragg positions (blue bars). (e) A HAADF-STEM image along the [20$\bar{1}$] zone axis. The blue balls show the positions of vanadium. (f) The EELS spectrum shows the V-L and O-K edges.

from 151 to 90 mAh·g^{-1} during the high voltage cycling while it fades slightly from 124 to 118 mAh·g^{-1} cycled in 3.0–4.3 V. Even cycled at higher rates like 0.5, 1, 2, 5, 10 C in 3.0–4.3 V, LVP still shows good cycling performance after 500 cycles with the specific capacity retention maintaining at 95%, 97.4%, 98.6%, 98.2%, and 98.1%, respectively (Figs. S3(a) and S3(b) in the ESM)). The high capacity retention is mainly due to the good structural reversibility in 3.0–4.3 V, which can be confirmed by the *in situ* XRD [16]. Moreover, the charge–discharge curves with a plateaus-like shape evolved to be a slopy shape in 3.0–4.8 V during the cycles, corresponding to a gradual evolution from a "two-phase" reaction to a "solid-solution" behavior, as indicated with the black arrow in Fig. 2(a). This is an intrinsic behavior rather than a polarization behavior as reported [25]. Figures 2(d) and 2(e) show the EIS spectra, which contain a well-defined semicircle followed by a liner portion. The semicircle reflects the charge transfer resistance (R_{ct}) and interfacial capacitance between the electrolyte and the active material while the liner part represents the Warburg impedance, associated with lithium ion diffusion in the LVP particles. In the voltage window 3.0–4.8 V, the R_{ct} increases from 179 to 790 Ω after 500 cycles (Fig. S4 in the ESM), likely due to the decomposition of the electrolyte and structure distortion, as confirmed in the following part. In contrast, the R_{ct} decreases from 84 to 24 Ω in the voltage window 3.0–4.3 V after 500 cycles called "activation" owning to a better contact between the electrolyte and the electrode [26, 27]. The impedance-decreased behavior can be observed at higher cycling rates in 3.0–4.3 V (Figs. S3(c) and S3(d) in the ESM) thus it promises good rate performances.

The decomposition of the electrolyte leads to the formation of the SEI layer. Figure S5 in the ESM shows the micromorphology and chemical composition of the SEI film. The thickness of the SEI film ranges from 48 to 113 nm of LVP after 500 cycles in 3.0–4.8 V while the thickness is about 20 nm when cycled in 3.0–4.3 V after 500 cycles as shown in in Fig. S5(a) and S5(b) in the ESM. The thicker SEI film also contributes to the increased R_{ct} of the LVP after 500 cycles in 3.0–4.8 V. The corresponding EDS mappings in Figs. S5(c) and S5(h) in the ESM further show the composition of the SEI film, which contains C, O, and F, referring to some inorganic compounds like Li_2CO_3, LiF and Li_2O and organic compounds such as $ROCO_2Li$, and RCO_2Li. The thick SEI film in 3.0–4.8 V shows inhomogeneous distribution, suggesting the instability and progressive formation of SEI layer, thus leading to the successive irreversible capacity loss, while the uniform SEI film in 3.0–4.3 V can ensure an excellent electrochemical performance.

To probe the electronic structures and chemical environments of LVP under high voltage cycling operations, we performed the EELS measurements as shown in Fig. 3. Note that EELS measurements were carried out on a cycled LVP in 3.0–4.8 V after 500 cycles, the valence of vanadium is expected to be +3. However, the EELS line scan profile shows a clear energy red-shift for the V-L_3 edge from the core to the surface (Figs. 3(a) and 3(b))), indicating a reduction of the vanadium valence [28]. The total edge red-shift is ~ 1.3 eV (Fig. 3(c)), which matches the reported V-L_3 edge red-shift from V_2O_5 to V_2O_3 (1.05 eV) [29] indicating a reduction from $V^{4.5+}$ to V^{3+} (considering that the lowest energy corresponds to the V^{3+} in LVP). According to the linear relationship between the energy onset and the oxidation state [30], we can acquire the oxidation state of V from V-L_3 onset energy (Fig. 3(c)), furthering obtaining the x values in $Li_{3-x}V_2(PO_4)_3$ ($Li_{3-x}VP$) (Fig. S6 in the ESM). We can observe a gradual decrease of x value in $Li_{3-x}VP$ towards the surface, indicating the inner part of the particle has already lost the electrochemical activity and Li-deficient phase tends to form at the core and gradually grows outward. This is mainly because under kinetic limitations, it is difficult for Li^+ to diffuse through numerous unit cells to arrive the core. Moreover, because of the lower ionic conductivity in Li-deficient phase [31], once Li-deficient phase is formed, it is more difficult for Li^+ to migrate through the Li-deficient phase. The Li-deficient phase shares similar crystallographic structure with $Li_3V_2(PO_4)_3$ [32, 33]. According to the practical specific capacity (90 mAh·g^{-1}) of LVP after 500 cycles, the average x in $Li_{3-x}VP$ is estimated to be ~ 1.6, which indicates the local measurement of chemistry from EELS is reasonable. After 500 cycles the core is consisted of $L_{3-x}VP$ phases. This is consistent with the previous study that the average valence of vanadium is higher than +3 after one cycle [14]. The valence decrease of vanadium is representative and

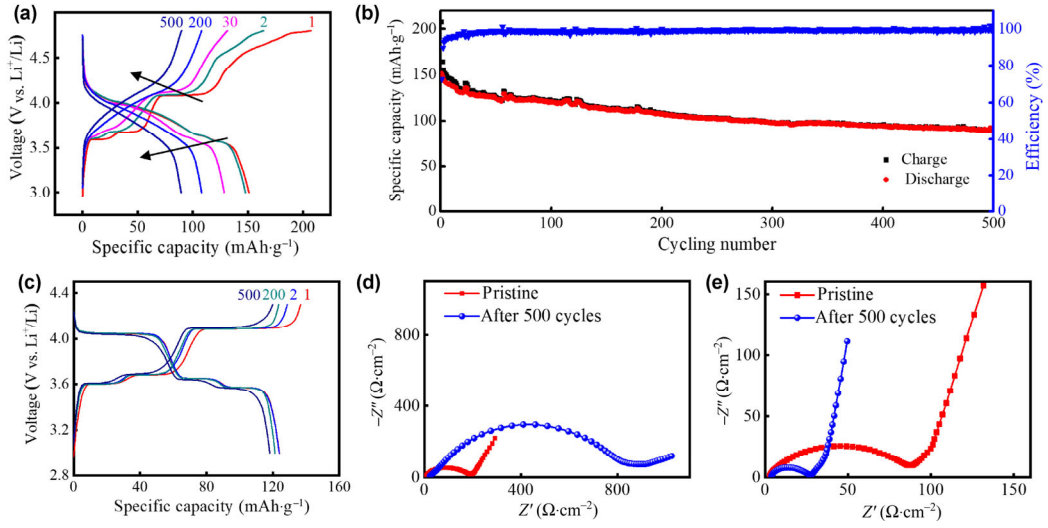

Figure 2 Battery cycling performance for LVP/C. (a) The charge/discharge voltage profiles of LVP cycling at 0.2 C in 3.0–4.8 V and (b) the corresponding cycling performance. (c) The charge/discharge voltage profiles of LVP cycling at 0.2 C in 3.0–4.3 V. (d) and (e) The Nyquist plots of impedance data from the cells before test and after 500 cycles cycling at 0.2 C in (d) 3.0–4.8 and (e) 3.0–4.3 V.

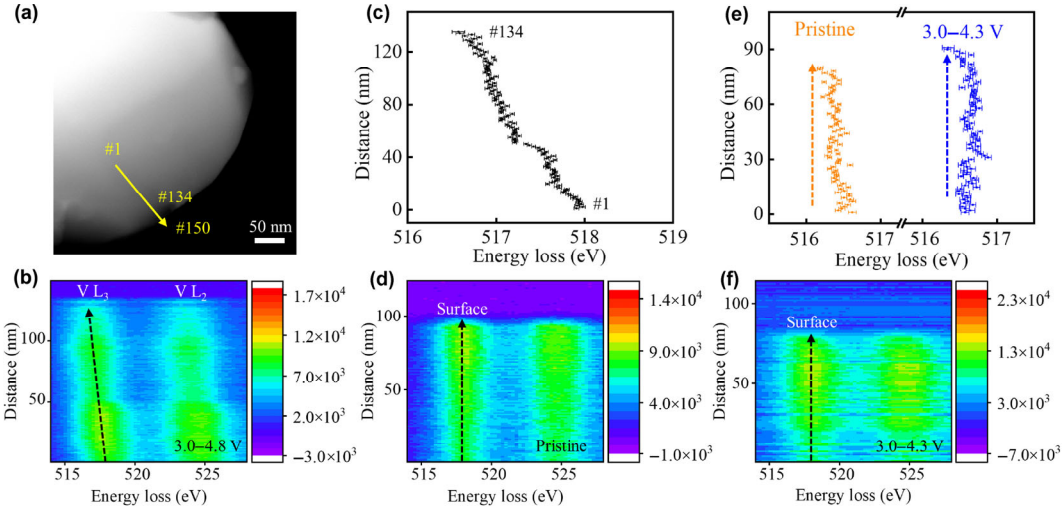

Figure 3 The chemical evolution for the LVP particle after 500 cycles in 3.0–4.8 V. (a) A STEM-HAADF image. The yellow arrow shows the line scan direction for acquiring the spectrum. (b) The corresponding 2D map to visualize the peak shift of V-L edges along the scanning direction. (c) The energy values of V-L_3 edge extracted from (b) as a function of distance. (d) and (f) The 2D maps of EELS line scan profiles of (d) the pristine LVP and (f) the cycled LVP at 0.2 C in the voltage range 3.0−4.3 V after 500 cycles. (e) The energy values of V-L_3 edge extracted from (d) and (f) as a function of distance, which shows a slight red-shift of the V-L_3 edge. The dashed arrows show the scanning direction.

another cycled LVP particle after 500 cycles in 3.0–4.8 V also shows a similar energy red-shift from the core to surface in Fig. S7 in the ESM. Note that the EELS line scan profiles for a pristine LVP and a cycled LVP in 3.0–4.3 V after 500 cycles demonstrate only slight shifts of the V-L_3 edge (Figs. 3(d)–3(f)).

Furthermore, we investigate the atomic structure of the LVP particle after 500 cycles at 0.2 C in 3.0–4.8 V as shown in Fig. 4. Atomically resolved STEM image in Fig. 4(a) shows the arrangement of vanadium along the [1$\bar{1}$0] direction, judging from the fast Fourier transform (FFT) pattern in Fig. 4(b). Compared with the simulated electron diffraction (ED) pattern of LVP in Fig. 4(c), the FFT pattern (Fig. 4(b)) presents additional (0 0 2k+1) superstructure spots. The superstructure spots have also been observed from (Fig. 4(d)) along the [1$\bar{2}$0] direction, whose ED pattern (Fig. 4(e)) shows additional reflections compared to the simulated ED pattern in Fig. S8 in the ESM. The superstructure reflections likely arise from the VO_6 octahedra distortion, which is common in oxide systems [34]. In our previous study based on the XAS [17], we can observe a significant increase of the pre-edge peaks, indicating the increase distortion of VO_6 octahedra due to a stronger 3d-4p mixing between metal 3d and ligand 2p orbitals [5]. It is reported for $Li_4Ti_5O_{12}$ that the local distortion of TiO_6 octahedra is related to the slight changes of Ti–O bond length (~ 0.2 Å) and the off-center displacements of Ti (0–0.2 Å) [35]. In our case, the distortion can be associated with the off-center displacements of vanadium, driven by the repulsive force between lithium ions and high oxidation state vanadium [36]. Note that such displacement is at the level of sub-angstrom [33, 35], which cannot directly be observed from the STEM image in Fig. 4(a). However, a previous *in situ* XAS study has confirmed the migration of vanadium to Li-vacancies based on the increased 1s-3d intensity [14]. Such lithium-vanadium anti-site mixing can block the lithium ion diffusion channel [37], leading to the formation of Li-deficient phase and the capacity loss due to the kinetics barriers under nonequilibrium condition, as evidenced in our previous study via galvanostatic intermittent titration technique and EIS a high electrochemical polarization can be observed in the transition from $Li_1V_2(PO_4)_3$ to $Li_0V_2(PO_4)_3$ [17]. It would be interesting to confirm the diffuse barrier by density-functional theory in the further study.

High resolution TEM (HRTEM) image in Fig. 4(f) shows the structure of the interface between the LVP and the Li-deficient phase

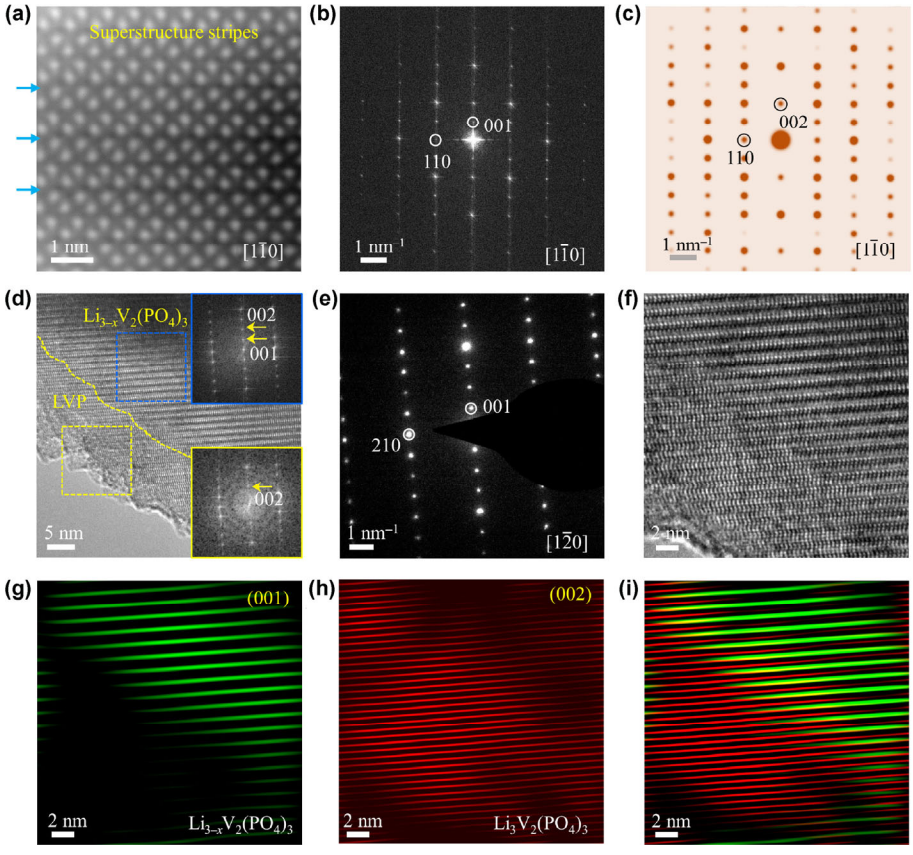

Figure 4 The structure of the LVP after 500 cycles at 0.2 C in 3.0–4.8 V. (a) A STEM image of the Li-deficient phase ($Li_{3-x}VP$). The darker layers indicated by the blue arrows show the superstructure stripes. (b) The corresponding FFT pattern showing additional reflections like (001) compared to that of (c) the simulated ED pattern of LVP along the [1$\bar{1}$0] zone axis. (d) A HRTEM image of surface structure along the [1$\bar{2}$0] direction. The inner layer is Li-deficient $Li_{3-x}VP$ with superstructure stripes while the out layer is LVP. Insets show the corresponding FFT patterns of LVP (yellow rectangular) and $Li_{3-x}VP$ (blue rectangular). (e) The corresponding SAED pattern with additional superstructure spots like (001). (f) An enlarged view of the HRTEM image and the corresponding inverse FFT patterns showing the distribution of (g) $Li_{3-x}VP$ using (002) diffraction spot and (h) LVP using (001) diffraction spot and (i) the combined patterns.

$L_{3-x}VP$. Based on the FFT patterns (inset of Fig. 4(d)), the inner layer with additional (001) reflections is identified to be $L_{3-x}VP$ while the outer layer is LVP with the width of ~ 5–10 nm. By choosing different reflections in the FFT pattern (inset of Fig. 4(d)), we can obtain the inverse FFT (IFFT) images, which show the spatial distributions of the Li-deficient $L_{3-x}VP$ (green) using (001) spots as a mask (Fig. 4(g)), LVP (red) using (002) spots as a mask (Fig. 4(h)) and the combination of both phases (Fig. 4(i)). The interface has also been observed along the [20$\bar{1}$] direction in Fig. S9 in the ESM with the LVP width ranging from 10 to 20 nm.

We mainly intend to probe the origin of the capacity loss based on the EELS, which, to best of our knowledge, has not been used in LVP cathode to investigate the capacity loss. Thus we hope to highlight the important role of EELS by the schematic diagram (Fig. 5) to further explain the capacity loss. The valence of vanadium in pristine LVP is +3. After charge–discharge cycles, the valence of vanadium is supposed to return to be +3. However, our EELS results show that the average valence of vanadium is higher than +3 cycled in 3.0–4.8 V. Specifically, for the LVP after 500 cycles, the valence of vanadium increases from the surface (+3) to the core (+4.5) when cycled in 3.0–4.8 V while the valence shows a homogeneous distribution as +3 when cycled in 3.0–4.3 V. Such valence evolution corresponds to the formation of Li-deficient phase (Fig. S6 in the ESM), which is likely caused by the migration of the vanadium, thus slowing down the lithium ion diffusion or even blocking the diffusion channels, leading to the final capacity loss.

To confirm this, lithium ion diffusion coefficients for LVP at various states have been calculated from the EIS data [38]. As shown in Table S1 in the ESM, the lithium ion diffusion coefficient is ~ 1.6×10^{-13} $cm^2 \cdot s^{-1}$ for the pristine LVP when cycled in 3.0–4.8 V while the diffusion coefficient decreases by an order of magnitude to be 4.8×10^{-14} $cm^2 \cdot s^{-1}$ after 500 cycles. In contrast, the diffusion coefficient increases from 6.9×10^{-13} to 3.8×10^{-12} $cm^2 \cdot s^{-1}$ after 500 cycles in 3.0–4.3 V owning to a better contact between the electrolyte and the electrode.

Further, it is of great importance to stabilize the structure and prevent the migration of vanadium to improve the capacity loss. Doping ions with large radii on V ion site helps to stabilize the monoclinic structure and buffer the volume changes during the

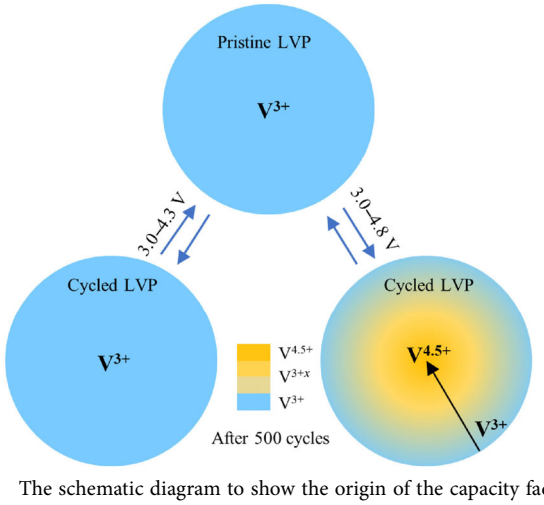

Figure 5 The schematic diagram to show the origin of the capacity fading for LVP cycling between electrochemical window 3.0–4.8 and 3.0–4.3 V.

cycles [39, 40]. Further, incorporating these foreign cations can also facilitate lithium ions transportation by creating defects or inducing lattice distortion with larger space and superionic channels [41–43]. With enhanced structure stability and ionic conductivity, doping on V ion site is supposed to prevent the formation of the electrochemically inactive Li-deficient phase and improve the capacity loss.

4 Conclusions

In summary, we focus on the microscopic electronic and atomic structures of pristine LVP and LVP after 500 cycles. EELS results show the valence of vanadium gradually increases towards the core, indicating that the surface LVP gradually evolves to the inner $V_2(PO_4)_3$ in 3.0–4.8 V. After 500 cycles, massive electrochemical inactive Li-deficient phase is formed while the width of LVP layer decreases to be only 5–20 nm. This Li-deficient phase is likely caused by the migration of the vanadium to Li vacancies, which can slow down the lithium ion diffusion or even block the diffusion channel. Such kinetic limitations explain the formation of the Li-deficient phase along with the capacity loss. The direct evidence of the core–shell structure, Li-deficient phase as well as inhomogeneous SEI layers can well explain the capacity fading mechanisms at an atomic level.

Acknowledgements

The work was supported by the National Natural Science Foundation of China (Nos. 51502032, 51575135, U1537206, 51502007, and 51672007), the National Basic Research Program of China (Nos. 2016YFA0300804 and 2016YFA0300903], and "2011 Program" Peking-Tsinghua-IOP Collaborative Innovation Center of Quantum Matter. We gratefully acknowledge Electron Microscopy Laboratory in Peking University for the use of Cs corrected electron microscope.

Electronic Supplementary Material: Supplementary material (morphologies EDS mappings, the electrochemical performance of the LVP/C, *x* values in Li-deficient phase, the chemical evolution of cycled LVP, the simulated electron diffraction and the interface between LVP and Li-deficient phase) is available in the online version of this article at https://doi.org/10.1007/s12274-019-2421-9.

References

[1] Goodenough, J. B.; Kim, Y. Challenges for rechargeable Li batteries. *Chem. Mater.* **2010**, *22*, 587–603.

[2] Kraytsberg, A.; Ein-Eli, Y. Higher, stronger, better… a review of 5 Volt cathode materials for advanced lithium-ion batteries. *Adv. Energy Mater.* **2012**, *2*, 922–939.

[3] Liu, H. W.; Cheng, C. X.; Huang, X. T.; Li, J. L. Hydrothermal synthesis and rate capacity studies of $Li_3V_2(PO_4)_3$ nanorods as cathode material for lithium-ion batteries. *Electrochim. Acta* **2010**, *55*, 8461–8465.

[4] Li, Y. Z.; Zhou, Z.; Ren, M. M.; Gao, X. P.; Yan, J. Electrochemical performance of nanocrystalline $Li_3V_2(PO_4)_3$/carbon composite material synthesized by a novel sol–gel method. *Electrochim. Acta* **2006**, *51*, 6498–6502.

[5] Gutierrez, A.; Qiao, R. M.; Wang, L. P.; Yang, W. L.; Wang, F.; Manthiram A. High-capacity, aliovalently doped olivine $LiMn_{1-3x/2}V_{x\square x/2}PO_4$ cathodes without carbon coating. *Chem. Mater.* **2014**, *26*, 3018–3026.

[6] Rui, X. H.; Yan, Q. Y.; Skyllas-Kazacos, M.; Lim, T. M. $Li_3V_2(PO_4)_3$ cathode materials for lithium-ion batteries: A review. *J. Power Sources* **2014**, *258*, 19–38.

[7] Wang, L. P.; Bai, J. M.; Gao, P.; Wang, X. Y.; Looney, J. P.; Wang, F. Structure tracking aided design and synthesis of $Li_3V_2(PO_4)_3$ nanocrystals as high-power cathodes for lithium ion batteries. *Chem. Mater.* **2015**, *27*, 5712–5718.

[8] Chen, Q. Q.; Wang, J. M.; Tang, Z.; He, W. C.; Shao, H. B.; Zhang, J. Q. Electrochemical performance of the carbon coated $Li_3V_2(PO_4)_3$ cathode material synthesized by a sol–gel method. *Electrochim. Acta* **2007**, *52*, 5251–5257.

[9] Luo, Y. Z.; Xu, X.; Zhang, Y. X.; Pi, Y. Q.; Zhao, Y. L.; Tian, X. C.; An, Q. Y.; Wei, Q. L.; Mai, L. Q. Hierarchical carbon decorated $Li_3V_2(PO_4)_3$ as a bicontinuous cathode with high-rate capability and broad temperature adaptability. *Adv. Energy Mater.* **2014**, *4*, 1400107.

[10] von Hagen, R.; Lepcha, A.; Song, X. F.; Tyrra, W.; Mathur, S. Influence of electrode design on the electrochemical performance of $Li_3V_2(PO_4)_3$/C nanocomposite cathode in lithium ion batteries. *Nano Energy* **2013**, *2*, 304–313.

[11] Zhang, X. F.; Kühnel, R. S.; Hu, H. T.; Eder, D.; Balducci, A. Going nano with protic ionic liquids-the synthesis of carbon coated $Li_3V_2(PO_4)_3$ nanoparticles encapsulated in a carbon matrix for high power lithium-ion batteries. *Nano Energy* **2015**, *12*, 207–214.

[12] Han, D. W.; Lim, S. J.; Kim, Y. I.; Kang, S. H.; Lee, Y. C.; Kang, Y. M. Facile lithium ion transport through superionic pathways formed on the surface of $Li_3V_2(PO_4)_3$/C for high power Li ion battery. *Chem. Mater.* **2014**, *26*, 3644–3650.

[13] Yoon, J.; Muhammad, S.; Jang, D.; Sivakumar, N.; Kim, J.; Jang, W. H.; Lee, Y. S.; Park, Y. U.; Kang, K.; Yoon, W. S. Study on structure and electrochemical properties of carbon-coated monoclinic $Li_3V_2(PO_4)_3$ using synchrotron based *in situ* X-ray diffraction and absorption. *J. Alloy. Compd.* **2013**, *569*, 76–81.

[14] Kim, S.; Zhang, Z. X.; Wang, S. L.; Yang, L.; Cairns, E. J.; Penner-Hahn, J. E.; Deb, A. Electrochemical and structural investigation of the mechanism of irreversibility in $Li_3V_2(PO_4)_3$ cathodes. *J. Phys. Chem. C* **2016**, *120*, 7005–7012.

[15] Min, X. J.; Huo, H.; Li, R. H.; Zhou, J. G.; Hu, Y. F.; Dai, C. S. Cycling stability of $Li_3V_2(PO_4)_3$/C cathode in a broad electrochemical window. *J. Electroanal. Chem.* **2016**, *774*, 76–82.

[16] Kang, J.; Mathew, V.; Gim, J.; Kim, S.; Song, J.; Im, W. B.; Han, J.; Lee, J. Y.; Kim, J. Pyro-synthesis of a high rate nano-$Li_3V_2(PO_4)_3$/C cathode with mixed morphology for advanced Li-ion batteries. *Sci. Rep.* **2014**, *4*, 4047.

[17] Wang, L. P.; Xu, J.; Wang, C.; Cui, X. M.; Li, J. Z.; Zhou, Y. N. A better understanding of the capacity fading mechanisms of $Li_3V_2(PO_4)_3$. *RSC Adv.* **2015**, *5*, 71684–71691.

[18] Williams, D. B.; Carter, C. B. *Transmission Electron Microscopy*; Plenum Press: New York, 1996.

[19] Yan, P. F.; Zheng, J. M.; Gu, M.; Xiao, J.; Zhang, J. G.; Wang, C. M. Intragranular cracking as a critical barrier for high-voltage usage of layer-structured cathode for lithium-ion batteries. *Nat. Commun.* **2017**, *8*, 14101.

[20] Yan, P. F.; Zheng, J. M.; Zhang, J. G.; Wang, C. M. Atomic resolution structural and chemical imaging revealing the sequential migration of Ni, Co, and Mn upon the battery cycling of layered cathode. *Nano Lett.* **2017**, *17*, 3946–3951.

[21] Lin, F.; Markus, I. M.; Nordlund, D.; Weng, T. C.; Asta, M. D.; Xin, H. L.; Doeff, M. M. Surface reconstruction and chemical evolution of stoichiometric layered cathode materials for lithium-ion batteries. *Nat. Commun.* **2014**, *5*, 3529.

[22] Yan, P. F.; Nie, A. M.; Zheng, J. M.; Zhou, Y. G.; Lu, D. P.; Zhang, X. F.; Xu, R.; Belharouak, I.; Zu, X. T.; Xiao, J. et al. Evolution of lattice structure and chemical composition of the surface reconstruction layer in $Li_{1.2}Ni_{0.2}Mn_{0.6}O_2$ cathode material for lithium ion batteries. *Nano Lett.* **2015**, *15*, 514–522.

[23] Zheng, J. M.; Gu, M.; Xiao, J.; Zuo, P. J.; Wang, C. M.; Zhang, J. G. Corrosion/fragmentation of layered composite cathode and related capacity/voltage fading during cycling process. *Nano Lett.* **2013**, *13*, 3824–3830.

[24] Pieczonka, N. P. W.; Liu, Z. Y.; Lu, P.; Olson, K. L.; Moote, J.; Powell, B. R.; Kim, J. H. Understanding transition-metal dissolution behavior in $LiNi_{0.5}Mn_{1.5}O_4$ high-voltage spinel for lithium ion batteries. *J. Phys. Chem. C* **2013**, *117*, 15947–15957.

[25] Huang, H.; Yin, S. C.; Kerr, T.; Taylor, N.; Nazar, L. F. Nanostructured composites: A high capacity, fast rate $Li_3V_2(PO_4)_3$/carbon cathode for rechargeable lithium batteries. *Adv. Mater.* **2002**, *14*, 1525–1528.

[26] Wang, L. P.; Zhang, L.; Wang, Q. J.; Li, W. J.; Wu, B.; Jia, W. S.; Wang, Y. H.; Li, J. Z.; Li, H. Long lifespan lithium metal anodes enabled by Al_2O_3 sputter coating. *Energy Storage Mater.* **2018**, *10*, 16–23.

[27] Wang, L. P.; Wang, Q. J.; Jia, W. S.; Chen, S. L.; Gao, P.; Li, J. Z. Li Metal coated with amorphous Li_3PO_4 via magnetron sputtering for stable and long-cycle life lithium metal batteries. *J. Power Sources* **2017**, *342*, 175–182.

[28] Horrocks, G. A.; Braham, E. J.; Liang, Y. F.; De Jesus, L. R.; Jude, J.; Velázquez, J. M.; Prendergast, D.; Banerjee, S. Vanadium K-edge X-ray absorption spectroscopy as a probe of the heterogeneous lithiation of V_2O_5: First-principles modeling and principal component analysis. *J. Phys. Chem. C* **2016**, *120*, 23922–23932.

[29] Lin, X. W.; Wang, Y. Y.; Dravid, V. P.; Michalakos, P. M.; Kung, M. C. Valence states and hybridization in vanadium oxide systems investigated by transmission electron-energy-loss spectroscopy. *Phys. Rev. B* **1993**, *47*, 3477–3481.

[30] Tan, H. Y.; Verbeeck, J.; Abakumov, A.; Van Tendeloo, G. Oxidation state and chemical shift investigation in transition metal oxides by EELS. *Ultramicroscopy* **2012**, *116*, 24–33.

[31] Yin, S. C.; Strobel, P. S.; Grondey, H.; Nazar, L. F. $Li_{2.5}V_2(PO_4)_3$: A room-temperature analogue to the fast-ion conducting high-temperature γ-phase of $Li_3V_2(PO_4)_3$. *Chem. Mater.* **2004**, *16*, 1456–1465.

[32] Patoux, S.; Wurm, C.; Morcrette, M.; Rousse, G.; Masquelier, C. A comparative structural and electrochemical study of monoclinic $Li_3Fe_2(PO_4)_3$ and $Li_3V_2(PO_4)_3$. *J. Power Sources* **2003**, *119–121*, 278–284.

[33] Yin, S. C.; Grondey, H.; Strobel, P.; Anne, M.; Nazar, L. F. Electrochemical property: Structure relationships in monoclinic $Li_{3-y}V_2(PO_4)_3$. *J. Am. Chem. Soc.* **2003**, *125*, 10402–10411.

[34] Woodward, D. I.; Reaney, I. M. Electron diffraction of tilted perovskites. *Acta Crystallogr., Sect. B: Struct. Sci.* **2005**, *61*, 387–399.

[35] Zhang, W.; Topsakal, M.; Cama, C.; Pelliccione, C. J.; Zhao, H.; Ehrlich, S.; Wu, L. J.; Zhu, Y. M.; Frenkel, A. I.; Takeuchi, K. J. et al. Multi-stage structural transformations in zero-strain lithium titanate unveiled by *in situ* X-ray absorption fingerprints. *J. Am. Chem. Soc.* **2017**, *139*, 16591–16603.

[36] Yin, S. C.; Grondey, H.; Strobel, P.; Huang, H.; Nazar, L. F. Charge ordering in lithium vanadium phosphates: Electrode materials for lithium-ion batteries. *J. Am. Chem. Soc.* **2003**, *125*, 326–327.

[37] Gao, P.; Ishikawa, R.; Tochigi, E.; Kumamoto, A.; Shibata, N.; Ikuhara, Y. Atomic-scale tracking of a phase transition from spinel to rocksalt in lithium manganese oxide. *Chem. Mater.* **2017**, *29*, 1006–1013.

[38] Wang, L.; Zhao, J. S.; He, X. M.; Gao, J.; Li, J. J.; Wan, C. R.; Jiang, C. Y. Electrochemical impedance spectroscopy (EIS) study of $LiNi_{1/3}Co_{1/3}Mn_{1/3}O_2$ for Li-ion batteries. *Int. J. Electrochem. Sci.* **2012**, *7*, 345–353.

[39] Sun, C. W.; Rajasekhara, S.; Dong, Y. Z.; Goodenough, J. B. Hydrothermal synthesis and electrochemical properties of $Li_3V_2(PO_4)_3$/C-based composites for lithium-ion batteries. *ACS Appl. Mater. Interfaces* **2011**, *3*, 3772–3776.

[40] Wang, W. H.; Zhang, J. L.; Jia, Z.; Dai, C. S.; Hu, Y. F.; Zhou, J. G.; Xiao, Q. F. Enhancement of the cycling performance of $Li_3V_2(PO_4)_3$/C by stabilizing the crystal structure through Zn^{2+} doping. *Phys. Chem. Chem. Phys.* **2014**, *16*, 13858–13865.

[41] Yuan, W.; Yan, J.; Tang, Z. Y.; Sha, O.; Wang, J. M.; Mao, W. F.; Ma, L. Mo-doped $Li_3V_2(PO_4)_3$/C cathode material with high rate capability and long term cyclic stability. *Electrochim. Acta* **2012**, *72*, 138–142.

[42] Zhang, S.; Wu, Q.; Deng, C.; Liu, F. L.; Zhang, M.; Meng, F. L.; Gao, H. Synthesis and characterization of Ti–Mn and Ti–Fe codoped $Li_3V_2(PO_4)_3$ as cathode material for lithium ion batteries. *J. Power Sources* **2012**, *218*, 56–64.

[43] Ren, M. M.; Zhou, Z.; Li, Y. Z.; Gao, X. P.; Yan, J. Preparation and electrochemical studies of Fe-doped $Li_3V_2(PO_4)_3$ cathode materials for lithium-ion batteries. *J. Power Sources* **2006**, *162*, 1357–1362.